Simultaneous determination of the second-harmonic generation emission directionality and reduced scattering coefficient from three-dimensional imaging of thick tissues

Gunnsteinn Hall
Kevin W. Eliceiri
Paul J. Campagnola

Simultaneous determination of the second-harmonic generation emission directionality and reduced scattering coefficient from three-dimensional imaging of thick tissues

Gunnsteinn Hall,[a,b] **Kevin W. Eliceiri,**[a] **and Paul J. Campagnola**[a,c]
[a]University of Wisconsin-Madison, Department of Biomedical Engineering and Laboratory of Optical and Computational Instrumentation, Madison, Wisconsin 53706
[b]Johns Hopkins University, Department of Biomedical Engineering, Baltimore, Maryland 21205
[c]University of Wisconsin-Madison, Department of Medical Physics, Madison, Wisconsin 53706

Abstract. Second-harmonic generation (SHG) microscopy has intrinsic contrast for imaging fibrillar collagen and has shown great promise for disease characterization and diagnostics. In addition to morphology, additional information is achievable as the initially emitted SHG radiation directionality is related to subresolution fibril size and distribution. We show that by two parameter fittings, both the emission pattern $(F_{SHG}/B_{SHG})_{creation}$ and the reduced scattering coefficient μ_s', can be obtained from the best fits between three-dimensional experimental data and Monte Carlo simulations. The improved simulation framework accounts for collection apertures for the detected forward and backward components. We apply the new simulation framework to mouse tail tendon for validation and show that the spectral slope of μ_s' obtained is similar to that from bulk optical measurements and that the $(F_{SHG}/B_{SHG})_{creation}$ values are also similar to previous results. Additionally, we find that the SHG emission becomes increasingly forward directed at longer wavelengths, which is consistent with decreased dispersion in refractive index between the laser and SHG wavelengths. As both the spectral slope of μ_s' and $(F_{SHG}/B_{SHG})_{creation}$ have been linked to the underlying tissue structure, simultaneously obtaining these parameters on a microscope platform from the same tissue provides a powerful method for tissue characterization. © *The Authors. Published by SPIE under a Creative Commons Attribution 3.0 Unported License. Distribution or reproduction of this work in whole or in part requires full attribution of the original publication, including its DOI.* [DOI: 10.1117/1.JBO.18.11.116008]

1 Introduction

Second-harmonic generation (SHG) microscopy has found great use in imaging a wide array of tissues that are either comprised primarily of collagen (e.g., connective tissues and cornea) or contain collagen as part of the extracellular matrix (e.g., stroma in breast, ovary, and colon).[1–10] There has been substantial interest in using this modality as a disease diagnostic for pathologies in such tissues, as the underlying contrast depends on the fibrillar organization, which can change in diseased states.[11,12] Many metrics have been developed to exploit these differences. For example, several image-processing techniques have been implemented for many conditions including cancers, connective tissue disorders, musculoskeletal conditions, and fibroses of internal organs.[13–20] Although often successful, such analyses typically depend on some degree of regularity in the image.

It is also possible to exploit the coherent nature of the SHG emission as a more general means to characterize tissue structure. Due to the underlying coherence of SHG, the size and packing of collagen fibrils within the focal volume lead to a specific spatial radiation pattern, i.e., a distribution of forward- and backward-created components, which we designate F_{SHG} and B_{SHG}, respectively, and define their ratio as the SHG creation ratio $(F_{SHG}/B_{SHG})_{creation}$.[21] This is in contrast to fluorescence where the emission pattern is spatially isotropic. It is also fundamentally different than SHG from uniaxial crystals [e.g., beta barium borate crystal (BBO) and potassium dihydrogen phosphate (KDP)], where the ideal phase matching between the laser and SHG wavelengths (i.e., $\Delta k = 0$) leads to entirely forward-propagating signals.

Several studies have compared the resulting forward and backward images from collagen in tissues and suggested models based on fibril size to interpret the data.[22–24] In a general model, we described how the spatial emission distribution is related to the phase-matching conditions, where we associated backward-emitted components with smaller and/or more randomly oriented fibrils (relative to λ_{SHG} in the axial direction).[21] We have used the SHG creation ratio as part of a metric to differentiate normal and diseased tissues in several cases including the connective tissue disorder, osteogenesis imperfecta (OI),[25] human ovarian cancer,[26] and *in vitro* models of breast cancer.[27] Burke et al.[28] also recently applied the concept in thin sections of breast cancer biopsies. Determination of the $(F_{SHG}/B_{SHG})_{creation}$ is important as it arises from subresolution fibril size ($\sim$50 to 200 nm) and packing.[21] Although it is not possible to achieve resolution at this level, inferences on the structure can still be determined.

There is additional richness in measuring the SHG directionality in tissues of thickness of more than one optical scattering length. Then, the measured F/B ratio as a function of depth is a compounded effect of the $(F_{SHG}/B_{SHG})_{creation}$, the scattering coefficient μ_s, and the scattering anisotropy g.[25] The former and latter parameters are related to density and organization,

Address all correspondence to: Paul J. Campagnola, University of Wisconsin-Madison, Department of Biomedical Engineering and Laboratory of Optical and Computational Instrumentation, Engineering Centers Building, 1550 Engineering Drive, Madison, Wisconsin 53706. Tel: (608) 890-3575; Fax: 608-265-9239; E-mail: pcampagnola@wisc.edu

respectively, and the spectral dependence of the reduced scattering coefficient $\mu_s' = \mu_s(1 - g)$ depends on the size and organization of scattering objects. For example, a steeper spectral slope corresponds to smaller and/or more random assemblies.[29] These optical parameters are another means to characterize differences in fibrillar structure in normal and diseased tissues.

The relative contributions of the SHG creation and subsequent propagation based on μ_s and g to the measured F/B are depth dependent and cannot be experimentally determined, as the detected photons from the two processes are indistinguishable. Monte Carlo simulation techniques are thus required to decouple the relative contributions. Our previous approach was to separately measure the depth dependence of the SHG F/B ratio and the bulk optical properties (via integrating spheres and goniometry) and then to run a series of simulations to obtain the best fit to $(F_{SHG}/B_{SHG})_{creation}$. We employed this approach for OI[25] and ovarian cancer,[26] and also in the analysis of optical clearing data.[30] We note that in diseased states, either or both the SHG creation and subsequent propagation can be different between tissues, and it is not possible to *a priori* predict differences. For example, in OI, the creation ratio was similar and the propagation was distinct,[25] whereas both were different in ovarian cancer.[26] Limiting aspects of this general approach are the need to measure the bulk optical properties separately and the highly averaged nature of the experiment.

It would be advantageous to perform both the SHG and optical property determinations on a microscope where the same part of the tissue would be simultaneously analyzed. Here, we report a new method that achieves this goal of obtaining $(F_{SHG}/B_{SHG})_{creation}$ and μ_s' from the measured F/B versus depth data combined with Monte Carlo simulations. We note that unlike the use of phantoms for optical scattering, analogous phantoms for SHG attributes do not currently exist. Ideally, phase-matched birefringent crystals with known nonlinear susceptibilities only produce forward-directed SHG. Self-assembled fibrillar collagen gels are often created as *in vitro* models; the extent of polymerization varies considerably between syntheses, and these are not true phantoms.[31] Instead, in this study, we used rat and mouse tail tendons for validation of the approach, as the SHG attributes have been the most extensively characterized of any tissues.[24,32–34]

To achieve this goal, we updated and improved the Monte Carlo simulation framework. Our previous approach[25] adapted the Monte Carlo Multi-Layered (MCML) framework[35] by adding optical sectioning, both primary and secondary filters, and the SHG-emitted creation ratio. However, it did not account for the collection apertures of the condenser and objectives for the forward and backward components, respectively. We show that the proper inclusion significantly affects the extracted $(F_{SHG}/B_{SHG})_{creation}$ values. To verify the approach, μ_s' was determined across a broad range of SHG wavelengths (445 to 615 nm), and we found results similar to those obtained by bulk measurements. We also obtained $(F_{SHG}/B_{SHG})_{creation}$ across corresponding laser excitation wavelengths and showed that it increases with increasing wavelength, where this result is consistent with phase-matching considerations.

2 Experimental Methods

2.1 Specimens and Preparation

Mouse tail tendons were extracted from wild-type Col1a1 mice and fixed in formalin for 24 h and then stored in phosphate buffered saline (PBS) at 4°C. It has been demonstrated that fixation does not alter the underlying fibrillar collagen structure and the resulting SHG properties[36–38] and primarily results in a slight volumetric shrinking.[39] For imaging, a single fascicle was pulled from the tail, and a small section was cut lengthwise, placed on a microscope slide with a drop of PBS, and sealed with a coverslip using nail polish (Sinful Colors). The samples varied in diameter from 60 to 90 μm. The thickness for each is estimated from the image data and the averaged z-profile intensity. Tendons were acquired from three mice, and three samples were imaged from each. As mouse tendons were too small to adequately fill the area of the laser spot in bulk measurements, rat tail tendons were used instead. Here, two to three rat tail tendons were used, where they were cut and folded out on a microscope slide to extend the width, and a coverglass was put on top to further increase the spread area and to ensure that all the space interacting with the laser was filled.

2.2 SHG Microscope and Measurements

The SHG microscope and data acquisition protocols have been described elsewhere.[40] Briefly, a Ti:Sapphire laser is coupled to a homebuilt laser-scanning system (WiscScan) on a fixed stage upright microscope base (Olympus, Center Valley, Pennsylvania BX61WI) microscope. A 40×0.8 numerical aperture (NA) water immersion objective and 0.9 NA condenser are used for excitation and collection, respectively, of the forward SHG signal. The backward SHG is collected in a nondescanned geometry, where the detector is in the infinity space. Both detection channels use Hamamatsu, Hamamatsu, Japan 7422-40P GaAsP photomultiplier tube (PMT)s. The calibration of the efficiencies of the forward and backward detection paths was obtained by two-photon excited fluorescence imaging of beads that emit in the same wavelength range as the detected SHG signal. The laser excitation wavelength range was 890 to 1230 nm and provided by a Coherent Chameleon, Santa Clara, California Ultra Ti:Sapphire oscillator (680 to 1080 nm tunability) and a synchronously pumped APE Optical Parametric Oscillator (1050 to 1700 nm tuning range). For all excitations, the corresponding SHG signal is filtered with 20-nm full width at half maximum bandpass filters (Semrock, Rochester, New York FF01-445/20, FF01-494/20, FF01-583/22, and FF01-615/20). The setup is designed such that both sources have the same beam size entering the microscope and follow the same optical path, allowing robust switching through two high-precision motorized stages. Circularly polarized light, as determined at the focus, is used throughout to avoid alignment specific effects.

The F/B versus depth measurement was made for the entire thickness of the tendon. Each was made in triplicate, where for each specimen the data was obtained sequentially across the wavelength range. The SHG intensities were integrated across the whole tendon. Image analysis was performed using FIJI (an open-source platform for biological-image analysis)[41] and MATLAB.

2.3 Bulk Optical Property Measurements

We recently described a new approach to bulk optical property measurements used to determine μ_s and g.[42] For fibrillar tissues with little absorption, such as the tendon used here, the overall attenuation can be approximated by μ_s alone, which we obtain through a measurement of the on-axis attenuation of the tissue

sample. Goniometry is used to determine the effective scattering anisotropy g_{eff}, which is reduced from the true single-scattering value when the tissue is more than one scattering length in thickness. With independent knowledge of μ_s and tissue thickness, a series of forward Monte Carlo simulations based on MCML[35] is used to obtain the best fit for the single-scattering anisotropy. The merged parameter μ_s' is then compared with that extracted through the measured SHG F/B versus depth response across the 890- to 1230-nm wavelength range.

2.4 Simulation Framework

We previously extended[25] the MCML framework[35] to allow for focusing of light and SHG creation directionality and conversion efficiency, as well as the primary and secondary filters effects on the SHG creation and propagation, respectively. As will be described in detail in Sec. 3.2, we now fit the simulated F/B response to simultaneously extract $(F_{SHG}/B_{SHG})_{creation}$ values and μ_s'. The new extended code was first validated in several ways. First, we verified that the modifications did not affect the original photon migration functionality by running several identical simulations that did not use any of the new features. Second, to validate the collection framework, we simulated isotropic fluorescence from within the sample and validated that the collection was as expected from the solid angle of the collection geometry (both forward and backward) in cases where no scattering or absorption was present and the refractive index mismatch of all layers was identical to avoid reflections. Third, to validate that the SHG directionality was modeled correctly, the detected SHG F/B was measured in
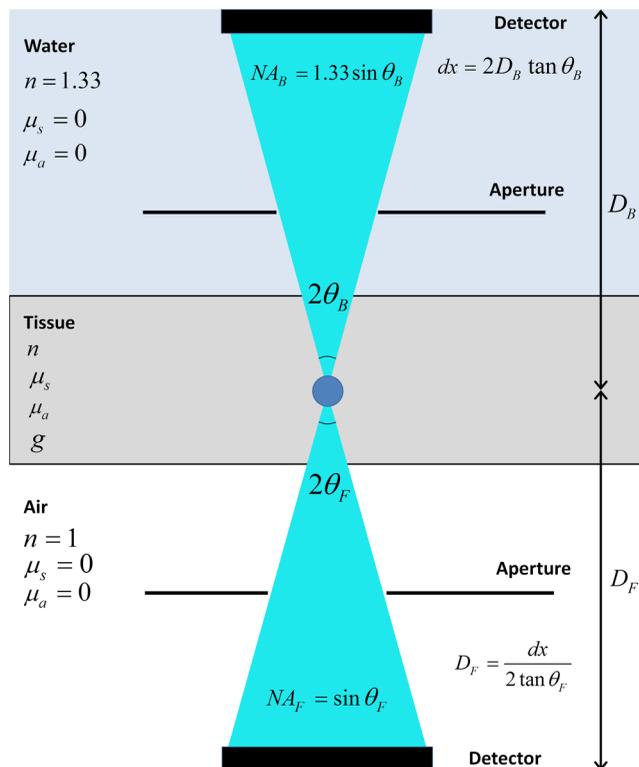
a nonabsorbing, nonscattering sample with no refractive index mismatch and was verified to be the same as the specified $(F_{SHG}/B_{SHG})_{creation}$.

In our previous treatment, no collection apertures were included in the modeling. Here, we have modified the simulations to account for the effect of the aperture, as multiply scattered photons can miss collection and result in erroneous F/B ratios. The available apertures in the backward and forward directions are defined by the NA of the objective and condenser lenses, respectively. The geometry used in the simulation is shown in Fig. 1. The simulation framework has a defined sampling width dx, i.e., constant for both the forward and backward geometries. We set $dx = 2D_B \tan\theta_B$ and $D_F = dx/2 \tan\theta_F$, where D_B and D_F denote the distances from the focus to the backward and forward detectors, respectively, and θ_F and θ_B are the collection angles defined by the condenser and objective for forward and backward SHG, respectively. In practice, the thickness of the sample is very thin compared with D_F, minimizing possible alignment artifacts. The Monte Carlo framework software is available upon request.
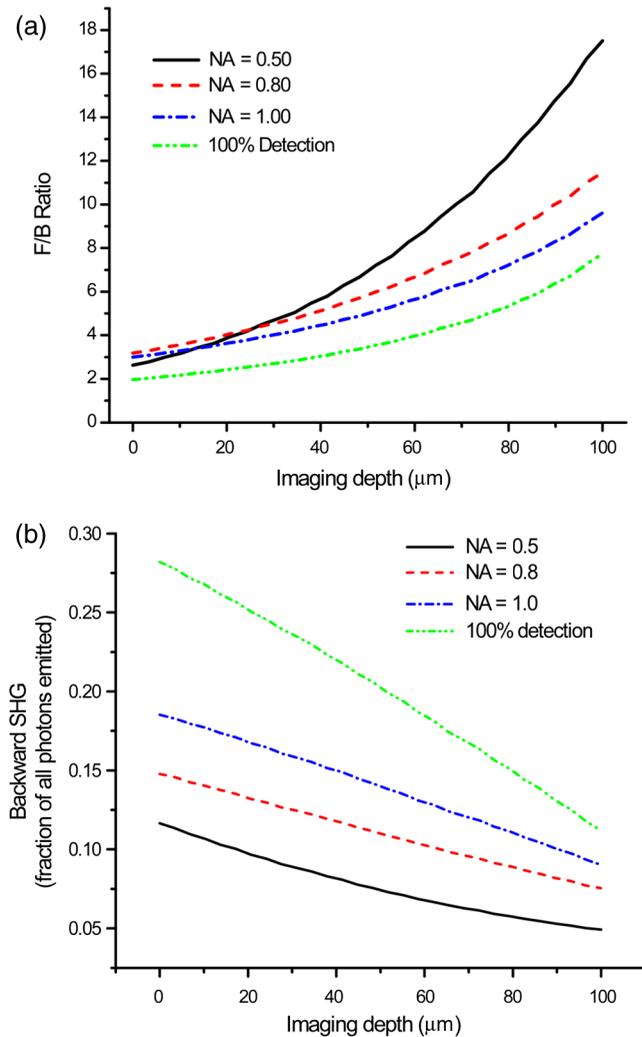
3 Results and Discussion

3.1 Effects of Collection Apertures and Optical Parameters on F/B Response

3.1.1 Effects of aperture size on the collection of forward and backward components

In prior work, we suggested that in tissues of 5 to 10 mean free path lengths for scattering in thickness, multiply scattered photons could be deviated at angles outside the NA of the collection optics.[30] Specifically, for the case of excitation becoming more proximal to the forward tissue exit, backward propagating photons would have an increasing probability of not being collected, resulting in an erroneously high F/B ratio. In our previous work,[25] we included the NA in the excitation to simulate optical sectioning; however, the respective forward and backward collection apertures were not included. Here, we updated the framework to this geometry and examined the effect on the resulting F/B ratios as a function of tissue thickness. Figure 2(a) shows the simulated F/B over 100 μm with excitation NA $= 0.8$ for 0.5 NA and 100% collection (as was previously assumed in the simulation) assuming typical parameters for tendon at 890 and 445 excitation and SHG emission, respectively,[30,43] where $F_{SHG}/B_{SHG} = 9$, $\mu_s = 450\ cm^{-1}$, $\mu_a = 10\ cm^{-1}$, and $g = 0.91$. Near the top entrance of the tissue ($z = 0$), the differences between the effective apertures are not significant but increase rapidly for excitation at greater depths. Specifically, at 100 μm into the tissue, the simulated F/B is much smaller using complete (and nonphysical) collection relative to that obtained the actual 0.8 NA by almost a factor of 1.5 (7 versus 11) due to missed photons in the backward channel. To further visualize this effect, consider the hypothetical case of 0.5 NA collection, where we observe apparent increasing (and artifactual) F/B near the bottom exit of the tissue as more backward propagating photons fail to become collected within this aperture. Thus, even for a relatively thin tissue of 100 μm of thickness, corresponding to ~2 mean free path lengths for scattering in tendon, this shows the importance of including the apertures within the simulation framework to accurately extract the emitted creation ratio from the experimental data.

We can also examine the effect of the objective NA on the measured attenuation of the backward-detected SHG as

Fig. 1 Monte Carlo simulation geometry for collection of the second-harmonic generation (SHG) signal, where D_B and D_F denote the distances from the focus to the backward and forward detectors, respectively, and θ_F and θ_B are the collection angles defined by the condenser and objective for forward and backward SHGs, respectively.

Fig. 2 Effects of collection aperture with 0.8 numerical aperture excitation on the depth-resolved forward/backward (F/B) (a) and backward attenuation (b) responses using previously determined bulk optical property measurements on tendon.

a function of excitation depth into the tissue. This response results from a combination of the square of the primary filter effect at the laser wavelength and the secondary filter effects at λ_{SHG}. Using the same conditions as in Fig. 2(a) and now including a primary filter effect of $\mu_s = 250$ cm^{-1}, Fig. 2(b) shows the resulting simulations over the same range of collection NAs. Here, assuming 100% collection underestimates, the rate of decay relative to that which would be measured using the 0.8 NA of the excitation/collection objective by approximately two-fold.

3.1.2 Effect of optical parameters on F/B measurement via Monte Carlo simulation

We now demonstrate the effect of the individual parameters $(F_{SHG}/B_{SHG})_{creation}$, μ_s, μ_a, and g on the F/B versus depth response when corrected for the collection apertures. Figure 3(a) illustrates simulated F/B ratios as a function of imaging depth z for increasing $(F_{SHG}/B_{SHG})_{creation}$ ratios over the range of 1 to 19 with typical μ_s, μ_a, and g values for the tendon. In the case of $F_{SHG}/B_{SHG} = 1$, the resulting F/B ratio is <1 at the tissue entrance due to scattering and becomes approximately the

SHG creation ratio in the mid-region of the tissue. For higher $(F_{SHG}/B_{SHG})_{creation}$ values, the $F/B(z) = (F_{SHG}/B_{SHG})_{creation}$ point is found increasingly toward the bottom of the sample. However, the location cannot be predicted fully analytically and, therefore, we need to utilize the Monte Carlo simulations using the measured bulk optical properties to obtain the $(F_{SHG}/B_{SHG})_{creation}$ values from the experimental data. Figure 3(b) illustrates the effect of varying only the scattering coefficient μ_s with other parameters fixed at comparable values, as we have previously reported for collagenous tissues. This primarily affects the slope of the resulting curve, with higher scattering coefficients resulting in steeper slopes. Figure 3(c) shows the effect of fixing the other parameters and varying the scattering anisotropy coefficient g, where this has a similar effect on strongly affecting the slope of the F/B curve. We have verified that different combinations of μ_s and g yielding the same μ_s' gave indistinguishable F/B versus depth curves for the same SHG creation ratio. This was performed for a range of μ_s' from 20 to 80 cm^{-1} with two representative combinations tested for each case (not shown). This verification affords extracting both $(F_{SHG}/B_{SHG})_{creation}$ and μ_s' from the measured F/B without the need for separate bulk optical property measurements (see Sec. 3.2). Figure 3(d) illustrates the effect of varying the absorption coefficient with the other parameters fixed. For collagenous tissues, the absorption is much weaker than scattering in this spectral region, and as a result, the curves in Fig. 3(d) are similar, showing that this parameter does not change the shape of the curve significantly and will be not be further considered in the analysis.

3.2 Obtaining both F_{SHG}/B_{SHG} and μ_s' from Fits to Depth-Resolved F/B Data

We next describe the simulation-based procedure of simultaneously obtaining $(F_{SHG}/B_{SHG})_{creation}$ and μ_s' from experimental F/B versus depth data without the need for separate bulk measurements. Figure 4(a) illustrates the process that generates tables of F/B values versus depth curves for a set of input parameters. We simulate $(F_{SHG}/B_{SHG})_{creation}$ from 1 to 20 in 100 steps and μ_s' from 5 to 50 cm^{-1} in 100 steps, and the F/B ratio is obtained at depths 0 to d in thickness in 30 steps. The simulations were performed on the Center for High Throughput Computing cluster at the University of Wisconsin, Madison. As the tendon samples varied somewhat in thickness, we generated seven separate tables with each thickness between 60 and 90 μm with a 5-μm step size. Figure 4(b) illustrates the data-processing steps required to obtain an experimental curve of F/B ratios, as a function of depth. We note that the process is averaged over the field-of-view after thresholding the image to eliminate background noise.

Figure 4(c) shows the full process of fitting the experimental data to the simulated curves to obtain values of μ_s' and $(F_{SHG}/B_{SHG})_{creation}$. This is done by calculating the reduced chi-squared coefficient between every simulated and experimental curve and determining the range of parameters that yield good fits to the experimental data, where the criterion of $\chi^2_{red} \leq 1$ is used and is calculated by

$$\chi^2_{red} = \frac{1}{\nu} \sum_{i=1}^{N} \frac{(F/B_{exp,i} - F/B_{sim,i})^2}{\sigma^2_{F/B}}, \quad (1)$$

where $\nu = N - P - 1$, N is the number of samples (slices at different depths), P is the number of fit parameters (typically
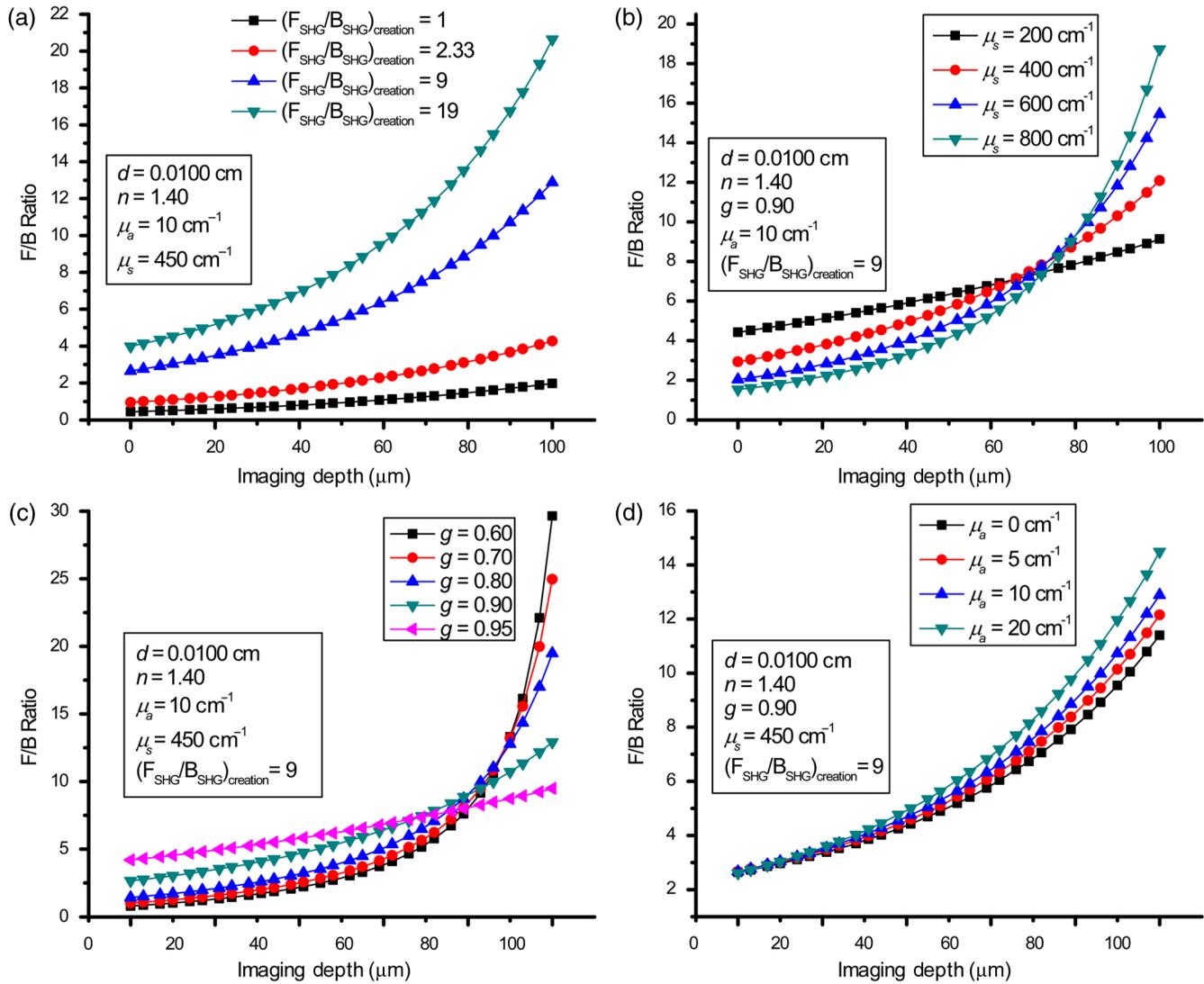
Fig. 3 Effects of the following optical parameters on the depth-resolved F/B ratio through simulations. (a) $F_{SHG}/B_{SHG\,creation}$, μ_s, g, and μ_a. Other parameters were kept fixed as indicated in each figure.

1 to 2), $F/B_{exp,i}$ is the experimental value at depth indexed by i, $F/B_{sim,i}$ is the corresponding simulated value, and last, $\sigma_{F/B}$ is the standard deviation of a single F/B measurement (calibrated) and is determined by the measurement uncertainty. Generally, the F/B value is obtained from a large number of pixels, requiring at least 2000 within the correct threshold. We estimated the error due to counting uncertainty by assuming an average of 30 counts per pixel in the forward direction, with a total count of ~60,000 (for 2000 pixels). The backward signal is found by dividing the forward count by the prescribed F/B ratio. The error is then estimated from $\sigma_{F/B} = [(F + \sqrt{F})/(B - \sqrt{B})] - [(F - \sqrt{F})/(B + \sqrt{B})]/2$. We find that under these assumptions, $\sigma_{F/B}$ increases steadily from 0.01 to 0.18 to 0.48 for increasing F/B ratios of 1, 10, and 20, respectively. Including these factors, we then estimate that $\sigma_{F/B} \approx 0.2$, which we will use to calculate the error (typical for F/B ratios of ~10, which are characteristic for this work). Another source of possible error is tissue inhomogeneity as the method assumes a homogeneous sample. Local sample inhomogeneities can cause nonmonotonic F/B versus depth responses; however, these effects are reduced when averaging over whole fields-of-view.

Moreover, the tendon is highly homogeneous in the context of real tissues.

In Fig. 5, we show representative fits of the experimental data to simulations at 890-nm excitation to obtain $(F_{SHG}/B_{SHG})_{creation}$ and μ_s'. In the simulations shown in Fig. 5(a), μ_s' was fixed, and the best fit for $(F_{SHG}/B_{SHG})_{creation}$ was found for three cases of the former via single-parameter fitting, where the acceptable fitting condition was $\chi_{red}^2 \leq 1$. Here, good fits were obtained for a range of μ_s' between 52 and 106 cm^{-1}, with a best fit at $\mu_s' = (79 \pm 25$ cm$^{-1})$. Analogous fits were performed for a several creation ratios between 5.8 and 6.76 with a range of μ_s' values (not shown). The best resulting fit $(F_{SHG}/B_{SHG})_{creation}$ was 6.3 ± 0.5 and similar to our previous results. The overall fitting results are shown in Fig. 5(b), where the $(F_{SHG}/B_{SHG})_{creation}$ and μ_s' are plotted with the corresponding χ_{red}^2 values. This shows that for good fits ($\chi_{red}^2 \leq 1$), the acceptable range of $(F_{SHG}/B_{SHG})_{creation}$ values is much narrower than for μ_s'. Therefore, we conclude that the method has higher sensitivity to extracting $(F_{SHG}/B_{SHG})_{creation}$ than for obtaining μ_s' values. However, the method does obtain both $(F_{SHG}/B_{SHG})_{creation}$ and μ_s' values
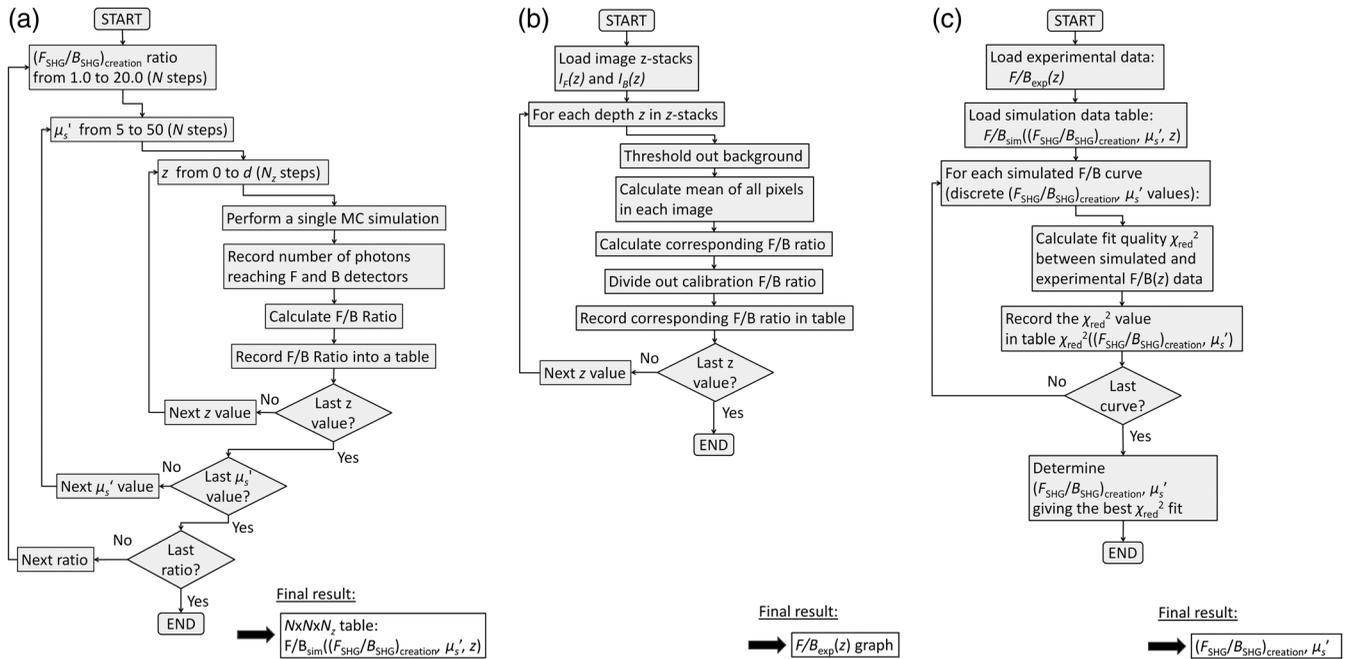
Fig. 4 Flowcharts illustrating the full process going from data acquisition to obtaining $(F_{SHG}/B_{SHG})_{creation}$ from fitting to simulations. (a) Generation of forward simulations, (b) loading of experimental data, and (c) fitting experimental to simulated data.
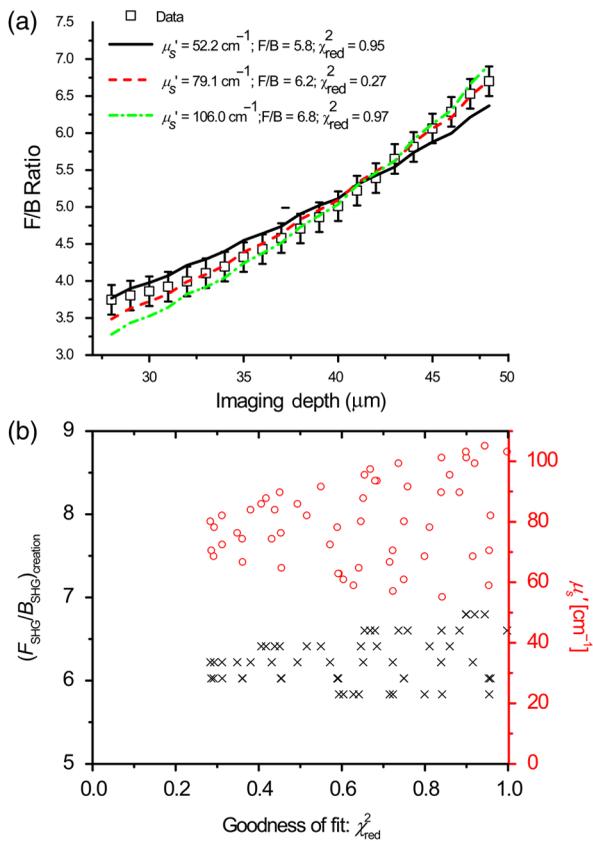

Fig. 5 Single example of fitting to the SHG creation ratio and reduced scattering coefficient for mouse tendon data. (a) Fits to several representative combinations of $(F_{SHG}/B_{SHG})_{creation}$ and μ_s' values with goodness of fit. The resulting best fits were $(F_{SHG}/B_{SHG})_{creation} = 6.3 \pm 0.5$ and $\mu_s' = 79 \pm 25$ cm^{-1} and (b) goodness of fits to $(F_{SHG}/B_{SHG})_{creation}$ and μ_s. A small range in creation ratios are obtained across a wider range of reduced scattering coefficients.

with acceptable fits based on the chi-squared criterion. We stress that the uncertainty in the μ_s' values does not significantly affect the obtained $(F_{SHG}/B_{SHG})_{creation}$ values, as all the best fits [Fig. 5(c)] are closely grouped around ~6 for a wide range of μ_s' values (50 to 100 cm^{-1}).

3.3 Spectral Slope Analysis

Figure 6 shows the dependence of the extracted reduced scattering coefficients from the SHG F/B data [hereafter denoted as $\mu_s'(SHG)$] over the range of SHG emission wavelength of 445 to 615 nm. This was initially performed for verification of the new analysis by comparison with prior bulk optical property measurements. However, if good agreement is obtained, this may obviate the need for separate bulk measurements for tissues that can be imaged on the SHG microscope. These data were averaged over several tissues, whereas the data and fits in Fig. 5 were the result of a single run. The Shapiro-Wilk test was run to determine if the data were normally distributed and if the Student t-test was appropriate for the analysis. This condition was satisfied, and Table 1 lists the p values from pairwise t-tests between the results for every combination of wavelengths. With the exception of 535 and 615 nm, the extracted $\mu_s'(SHG)$ values are statistically different at the $p < 0.05$ level. Thus, we conclude that the trend of decreasing μ_s' with increasing wavelength was statistically significant.

Table 2 lists the values as obtained by conventional bulk optical property measurements[22] (μ_s') and the fitting procedure from the SHG F/B data [$\mu_s'(SHG)$]. We note that the bulk optical property measurements were done on rat tail tendon rather than mouse tail tendon, as the latter is too small for complete overlap with the ~1-mm laser spot even when unwrapped and flattened. Moreover, the former is too thick to image in its entirety. However, transmission electron microscopy of both mouse and rat tails suggests that they have a similar distribution in fibril diameters.[44,45] As both SHG and scattering properties

(a)

$$\mu_s'(\lambda) = a(\lambda/500 \text{ nm})^b$$

$$a = 60 \pm 10 \text{ cm}^{-1}$$

$$b = -2.8 \pm 0.1$$

(b)
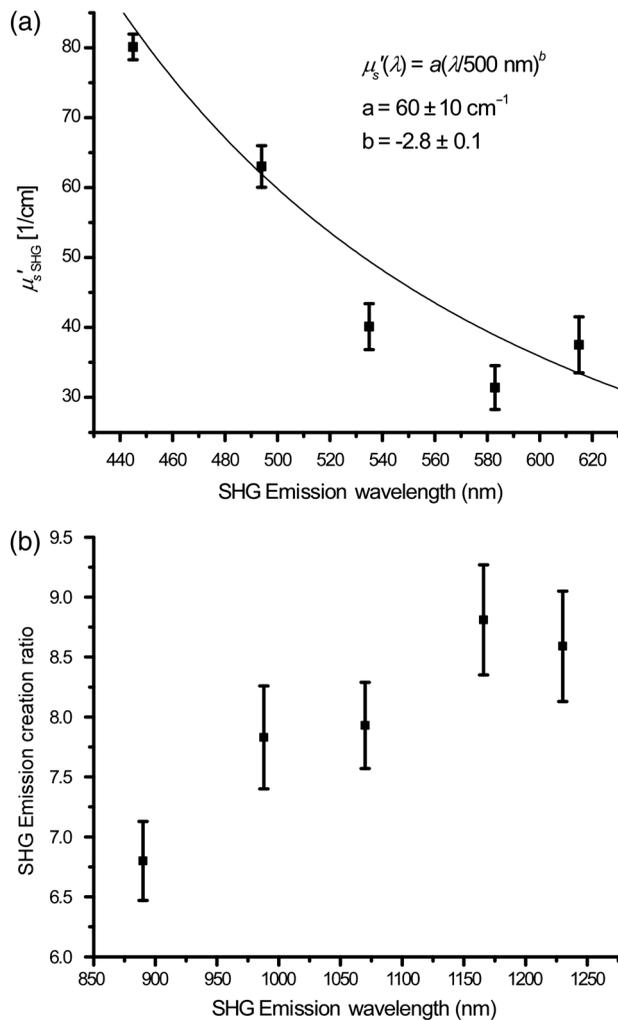
Fig. 6 Wavelength dependency of (a) μ_s' and (b) SHG creation ratio. Dataset for three different samples at three spots in each case. The error bars shown are the standard error of the mean.

are governed by the fibrillar structure, their respective attributes are also expected to be similar. Moreover, the fibrillar structures of these tissues are similar when viewed in the SHG microscope.

By comparing the tabulated data, we found that the $\mu_s'(\text{SHG})$ is roughly a factor of 2.5 times larger than μ_s' at the wavelengths listed (with some nonsystematic variations). This indicates that the wavelength dependence of both factors is linearly related by

Table 1 Results of pairwise *t*-tests for the best fits of μ_s' data between the different wavelength groups, where $p < 0.05$ values were considered to be statistically different. Only the 535 and 615-nm points were not significantly different.

	445 nm	494 nm	535 nm	583 nm	615 nm
445		0.0002	0	0	0
494			0.0022	0.0012	0.0176
535				0.0123	0.7183
583					0.0312
615					

Table 2 Comparison of the reduced scattering coefficient as obtained by bulk optical property measurements and retrieved from fits. The uncertainty is the standard deviation.

λ (nm)	μ_s' (cm^{-1})	μ_s'(SHG) (cm^{-1})
445	41 ± 11	91 ± 10
494	23 ± 9	64 ± 12
535	17 ± 5	43 ± 9
583		34 ± 14
615		42 ± 19
680	17 ± 4	

a constant coefficient. We have verified this by fitting the results to the power law $\mu_s'(\lambda) = a(\lambda/500 \text{ nm})^b$ over the same wavelength range. This best fit showed that the a factor increased by roughly a factor of 2.5 (80 ± 29 versus $31.2 \pm 9.6 \text{ cm}^{-1}$), whereas the scattering power b was not significantly different (2.8 ± 0.2 versus 2.7 ± 0.2).

We propose two possible reasons for the difference in scattering magnitude extracted by the two methods: (1) the local environment around the SHG creation region has a higher "local" scattering coefficient than the bulk due to dense fibril structure which is required for efficient SHG, which further has a quadratic dependence on concentration, i.e., less dense regions may contribute to the bulk μ_s' but not to the SHG signal; and (2) the radiation pattern of SHG emission is not directly on axis in the forward and backward directions, but instead has an angular distribution with a defined "phase function" (emission intensity as function of radiation angle). In this case, a higher number of emission scattering events would be required to emulate the experimental data, which only integrates forward and backward intensities within the NA of the condenser and objective, respectively. Our observations are consistent with either explanation. We note that the somewhat limited number of data points over a fairly broad wavelength range and relatively large uncertainty does not allow for highly accurate power-law fitting. Moreover, the resulting power law dependencies have been shown to depend on the range of wavelengths used for fitting.[46] However, based on theoretical modeling by Rogers et al.,[47] the spectral dependence or spectral slope of μ_s' carries the structural information related to scatter size and packing, more so than the absolute values. Indeed, the b coefficients reflecting the spectral slope were similar for both methods (2.8 versus 2.7).

Further studies are required to fully analyze and understand the reason for the higher $\mu_s'(\text{SHG})$ values. Such studies of the precise shape of the radiation pattern might also be of interest for a wide variety of studies and could give more information to the underlying tissue structure rather than just the relative strength of the F/B ratios. We emphasize that the obtained $\mu_s'(\text{SHG})$ may be useful for differentiating diseased versus normal tissues. For example, our limited data (two wavelengths) comparing μ_s' between normal and ovarian cancer showed a marked difference in spectral slope.[26] We also extracted marked differences in the SHG creation ratio and have seen large differences in the fibrillar morphology. Thus, it would be advantageous to simultaneously acquire SHG image data and concurrently extract

$(F_{SHG}/B_{SHG})_{creation}$ and the spectral slope of μ_s' as a generalized means to classify tissue.

3.4 *Wavelength Dependence of* $(F_{SHG}/B_{SHG})_{creation}$

Figure 6(b) shows the resulting wavelength dependency of the $(F_{SHG}/B_{SHG})_{creation}$ values for mouse tail tendon samples. The Shapiro-Wilk test showed that the data were normally distributed, and *t*-tests were used here for statistical analysis, as in Sec. 4. Paired *t*-tests between the different groups, listed in Table 3, show that all the measured creation ratios are statistically significantly ($p < 0.05$) different with two nonsystematic exceptions. Thus, we conclude that the trend of increasing $(F_{SHG}/B_{SHG})_{creation}$ values with increasing wavelength was statistically significant.

This increasing ratio is indicative of the phase mismatch $\Delta k = k_{2\omega} - 2k_\omega$ decreasing with increasing wavelength. In SHG microscopy, this mismatch is determined by the harmonophore distribution and associated spatial frequencies, the Gouy phase shift, and dispersion between the laser and SHG wavelengths.[21,48] Although the relative contributions of these factors are not yet fully understood, the overall trend is consistent with the reduced dispersion at longer wavelengths, as Δk decreases and the emission becomes more forward directed, i.e., has a longer coherence length.

This finding is in contrast to other papers examining the wavelength dependence of the SHG creation ratio. For example, recently Shen et al.[49] found no wavelength dependent effects and speculated that the backward signal arose from reflections of forwarded emitted SHG. We believe this is unlikely as completely forward-directed emission would require type I or II phase-matching conditions where $\Delta k = 0$. Such conditions do not exist in collagen. In further contrast, Theodossiou et al.[50] found differing wavelength dependencies for the forward and backward responses and used quasi-phase matching arguments to explain their findings. We note that these two studies utilized very thin sections of a few microns in thickness. Although the results from such specimens are nominally free of scattering, cutting effects can result in highly spatially dependent densities and be in significant differences in the measured F/B. We have not been able to obtain consistent results from such thin sections, and we posit that more accurate measurements are obtained from intact tissues with proper accounting of the scattering.

Table 3 Results of pairwise *t*-tests for the best fits of $(F_{SHG}/B_{SHG})_{creation}$ data between the different wavelength groups, where $p < 0.05$ values were considered to be statistically different. Statistically insignificant p values have been marked for clarification.

	890 nm	988 nm	1070 nm	1166 nm	1230 nm
890		0.0008	0.0001	0.0001	0.0004
988			0.3352	0.001	0.0172
1070				0.001	0.0229
1166					0.1304
1230					

4 Conclusions

We have constructed a Monte Carlo simulation model of three-dimensional SHG imaging data that allows for simultaneous extraction of the SHG emission creation ratio $(F_{SHG}/B_{SHG})_{creation}$ and the reduced scattering coefficient μ_s' from depth-dependent measurement of the experimental forward-backward ratio. By comparison with bulk optical measurements performed across a broad-wavelength range, the extracted μ_s' values from the SHG microscope measurement were ~2.5-fold larger than that obtained from bulk optical property measurements. However, the spectral slopes were similar for both methods, and it has been suggested that the quantity is more directly related to tissue structure than the absolute value. Further studies of the radiation pattern will be required to fully understand that mechanism. We suggest that this combined approach of obtaining SHG and scattering attributes simultaneously on the same microscope platform will provide general and powerful approach for analyzing tissue structure, as there are no underlying assumptions as are necessary for morphological- or polarization-based analyses. When applied across a broad-wavelength range, we expect this approach to be broadly applicable to differentiating normal and diseased tissues, as the respective SHG and scattering attributes may have different spectral dependencies.

References

1. P. J. Campagnola et al., "Three-dimensional high-resolution second-harmonic generation imaging of endogenous structural proteins in biological tissues," *Biophys. J.* **82**(1), 493–508 (2002).
2. W. Lo et al., "Intact corneal stroma visualization of GFP mouse revealed by multiphoton imaging," *Microsc. Res. Tech.* **69**(12), 973–975 (2006).
3. P. P. Provenzano et al., "Collagen density promotes mammary tumor initiation and progression," *BMC Med.* **6**, 11 (2008).
4. S. Y. Chen et al., "*In vivo* virtual biopsy of human skin by using non-invasive higher harmonic generation microscopy," *IEEE J. Sel. Top. Quantum Electron.* **16**(3), 478–492 (2010).
5. E. Brown et al., "Dynamic imaging of collagen and its modulation in tumors in vivo using second-harmonic generation," *Nat. Med.* **9**(6), 796–800 (2003).
6. R. Cicchi et al., "Basal cell carcinoma imaging and characterization by multiple nonlinear microscopy techniques," *Biophys. J.* 157a (2007).
7. M. Strupler et al., "Second harmonic imaging and scoring of collagen in fibrotic tissues," *Opt. Express* **15**(7), 4054–4065 (2007).
8. C. P. Pfeffer, B. R. Olsen, and F. Legare, "Second harmonic generation imaging of fascia within thick tissue block," *Opt. Express* **15**(12), 7296–7302 (2007).
9. K. G. Brockbank et al., "Quantitative second harmonic generation imaging of cartilage damage," *Cell Tissue Banking* **9**(4), 299–307 (2008).
10. G. P. Kwon et al., "Contribution of macromolecular structure to the retention of low-density lipoprotein at arterial branch points," *Circulation* **117**(22), 2919–2927 (2008).
11. P. Campagnola, "Second harmonic generation imaging microscopy: applications to diseases diagnostics," *Anal. Chem.* **83**(9), 3224–3231 (2011).

12. P. J. Campagnola and C. Y. Dong, "Second harmonic generation microscopy: principles and applications to disease diagnosis," *Lasers Photonics Rev.* **5**(1), 13–26 (2011).

13. R. Cicchi et al., "Scoring of collagen organization in healthy and diseased human dermis by multiphoton microscopy," *J. Biophotonics* **3**(1–2), 34–43 (2010).

14. S. Plotnikov et al., "Optical clearing for improved contrast in second harmonic generation imaging of skeletal muscle," *Biophys. J.* **90**(1), 328–339 (2006).

15. S. V. Plotnikov et al., "Measurement of muscle disease by quantitative second-harmonic generation imaging," *J. Biomed. Opt.* **13**(4), 044018 (2008).

16. A. M. Pena et al., "Three-dimensional investigation and scoring of extracellular matrix remodeling during lung fibrosis using multiphoton microscopy," *Microsc. Res. Tech.* **70**(2), 162–170 (2007).

17. W. Sun et al., "Nonlinear optical microscopy: use of second harmonic generation and two-photon microscopy for automated quantitative liver fibrosis studies," *J. Biomed. Opt.* **13**(6), 064010 (2008).

18. M. W. Conklin et al., "Aligned collagen is a prognostic signature for survival in human breast carcinoma," *Am. J. Pathol.* **178**(3), 1221–1232 (2011).

19. A. Ghazaryan et al., "Analysis of collagen fiber domain organization by Fourier second harmonic generation microscopy," *J. Biomed. Opt.* **18**(3), 031105 (2013).

20. K. M. Reiser et al., "Quantitative analysis of structural disorder in intervertebral disks using second harmonic generation imaging: comparison with morphometric analysis," *J. Biomed. Opt.* **12**(6), 064019 (2007).

21. R. Lacomb et al., "Phase matching considerations in second harmonic generation from tissues: effects on emission directionality, conversion efficiency and observed morphology," *Opt. Commun.* **281**(7), 1823–1832 (2008).

22. R. M. Williams, W. R. Zipfel, and W. W. Webb, "Interpreting second-harmonic generation images of collagen I fibrils," *Biophys. J.* **88**(2), 1377–1386 (2005).

23. M. Han, G. Giese, and J. F. Bille, "Second harmonic generation imaging of collagen fibrils in cornea and sclera," *Opt. Express* **13**(15), 5791–5797 (2005).

24. F. Legare, C. Pfeffer, and B. R. Olsen, "The role of backscattering in SHG tissue imaging," *Biophys. J.* **93**(4), 1312–1320 (2007).

25. R. Lacomb, O. Nadiarnykh, and P. J. Campagnola, "Quantitative SHG imaging of the diseased state osteogenesis imperfecta: experiment and simulation," *Biophys. J.* **94**(11), 4504–4514 (2008).

26. O. Nadiarnykh et al., "Alterations of the extracellular matrix in ovarian cancer studied by second harmonic generation imaging microscopy," *BMC Cancer* **10**, 94 (2010).

27. V. Ajeti et al., "Structural changes in mixed Col I/Col V collagen gels probed by SHG microscopy: implications for probing stromal alterations in human breast cancer," *Biomed. Opt. Express* **2**(8), 2307–2316 (2011).

28. K. Burke, P. Tang, and E. Brown, "Second harmonic generation reveals matrix alterations during breast tumor progression," *J. Biomed. Opt.* **18**(3), 031106 (2013).

29. Y. Liu et al., "Optical markers in duodenal mucosa predict the presence of pancreatic cancer," *Clin. Cancer Res.* **13**(15 Pt 1), 4392–4399 (2007).

30. R. LaComb et al., "Quantitative SHG imaging and modeling of the optical clearing mechanism in striated muscle and tendon," *J. Biomed. Opt.* **13**(2), 021108 (2008).

31. C. B. Raub et al., "Noninvasive assessment of collagen gel microstructure and mechanics using multiphoton microscopy," *Biophys. J.* **92**(6), 2212–2222 (2007).

32. I. Gusachenko et al., "Polarization-resolved second-harmonic generation in tendon upon mechanical stretching," *Biophys. J.* **102**(9), 2220–2229 (2012).

33. P. Stoller et al., "Polarization-dependent optical second-harmonic imaging of a rat-tail tendon," *J. Biomed. Opt.* **7**(2), 205–214 (2002).

34. X. X. Han and E. Brown, "Measurement of the ratio of forward-propagating to back-propagating second harmonic signal using a single objective," *Opt. Express* **18**(10), 10538–10550 (2010).

35. L. Wang, S. L. Jacques, and L. Zheng, "MCML–Monte Carlo modeling of light transport in multi-layered tissues," *Comput. Methods Programs Biomed.* **47**(2), 131–146 (1995).

36. O. Nadiarnykh et al., "Second harmonic generation imaging microscopy studies of osteogenesis imperfecta," *J. Biomed. Opt.* **12**(5), 051805 (2007).

37. A. Zoumi et al., "Imaging coronary artery microstructure using second-harmonic and two-photon fluorescence microscopy," *Biophys. J.* **87**(4), 2778–2786 (2004).

38. S. M. Kakkad et al., "Collagen I fiber density increases in lymph node positive breast cancers: pilot study," *J. Biomed. Opt.* **17**(11), 116017 (2012).

39. K. M. Meek, "The use of glutaraldehyde and tannic acid to preserve reconstituted collagen for electron microscopy," *Histochemistry* **73**(1), 115–120 (1981).

40. X. Chen et al., "Second harmonic generation microscopy for quantitative analysis of collagen fibrillar structure," *Nat. Protoc.* **7**(4), 654–669 (2012).

41. J. Schindelin et al., "Fiji: an open-source platform for biological-image analysis," *Nat. Methods* **9**(7), 676–682 (2012).

42. G. Hall et al., "Goniometric measurements of thick tissue using Monte Carlo simulations to obtain the single scattering anisotropy coefficient," *Biomed. Opt. Express* **3**(11), 2707–2719 (2012).

43. O. Nadiarnykh and P. J. Campagnola, "Retention of polarization signatures in SHG microscopy of scattering tissues through optical clearing," *Opt. Express* **17**(7), 5794–5806 (2009).

44. A. Corsi et al., "Phenotypic effects of biglycan deficiency are linked to collagen fibril abnormalities, are synergized by decorin deficiency, and mimic Ehlers-Danlos-like changes in bone and other connective tissues," *J. Bone Miner. Res.* **17**(7), 1180–1189 (2002).

45. D. A. Parry and A. S. Craig, "Quantitative electron microscope observations of the collagen fibrils in rat-tail tendon," *Biopolymers* **16**(5), 1015–1031 (1977).

46. A. N. Bashkatov et al., "Optical properties of human skin, subcutaneous and mucous tissues in the wavelength range from 400 to 2000 nm," *J. Phys. D-Appl. Phys.* **38**(15), 2543–2555 (2005).

47. J. D. Rogers, I. R. Capoglu, and V. Backman, "Nonscalar elastic light scattering from continuous random media in the Born approximation," *Opt. Lett.* **34**(12), 1891–1893 (2009).

48. J. Mertz and L. Moreaux, "Second-harmonic generation by focused excitation of inhomogeneously distributed scatterers," *Opt. Commun.* **196**(1–6), 325–330 (2001).

49. M. Shen et al., "Calibrating the measurement of wavelength-dependent second harmonic generation from biological tissues with a BaB(2)O(4) crystal," *J. Biomed. Opt.* **18**(3), 031109 (2013).

50. T. A. Theodossiou et al., "Second harmonic generation confocal microscopy of collagen type I from rat tendon cryosections," *Biophys. J.* **91**(12), 4665–4677 (2006).